Jingli Zhang*, Hongzhen Guo and Houquan Liang

Dynamic Recrystallization Behavior of Ti22Al25Nb Alloy during Hot Isothermal Deformation

DOI 10.1515/htmp-2015-0146
Received June 30, 2015; accepted November 5, 2015

Abstract: Dynamic recrystallization (DRX) of Ti22Al25Nb alloy has been investigated based on the analysis of hot compression experimental data in this paper. The true stress–strain curves of Ti22Al25Nb can be divided into two types: the single-peak conventional dynamic recrystallization (CDRX) curves and the multi-peak discontinuous dynamic recrystallization (DDRX) curves. The multi-peak curves indicate the alternate dominance of hardening mechanism and softening mechanism. A critical Zener–Hollomon parameter ln Z_C has been proposed to divide CDRX from DDRX. The hardening rate and DRX volume fraction of CDRX and DDRX have been analyzed. In addition, the effect of the second-phase particle on the DRX has been studied. DRX process was enhanced by the second-phase particles, but the growth process of recrystallized grains was restrained.

Keywords: titanium, dynamic recrystallization, hardening, softening, microstructure

PACS® (2010). 64.70.kd

Introduction

Ti2AlNb alloys, since they were found by Banerjee [1], have been extensively studied by researchers [2–6]. Due to the high strength and the excellent creep and oxidation resistance [7], these alloys have been widely used in high-temperature structural applications [8–10]. Differing from the conventional titanium alloys, the Ti2AlNb alloys mainly consist of different proportions of the body-centered-cubic (bcc) B2 phase matrix, the orthorhombic O phase and the close-packed hexagonal α_2 phase [11]. When deformed at the room temperature, Ti2AlNb alloys often exhibit poor properties because the α_2/B2 and O/B2 grain boundaries provide crack initiation sites, which are detrimental to strength and elongation [12–14]. During the hot deformation, the appropriate α_2/O vol pct can enhance the dynamic recrystallization (DRX) process [7], then the properties of Ti2AlNb alloys can be greatly improved [15–17].

DRX has been used widely to obtain the fine microstructure [18, 19]. During the DRX process, new dislocation-free grains will be formed within the deformed original structure, then grow and consume the old grains, which will result in a new microstructure with a low dislocation density. DRX, as well as work hardening (WH) and dynamic recovery (DRV), which lead to the microstructural evolution of deformed metals, can be directly reflected from the stress–strain curves. Mirzadeh et al. [20] modeled DRX process by the Johnson–Mehl–Avrami–Kolmogorov (JMAK) kinetics equation and proposed the dependence of DRX process on strain rate, deformation temperature and strain. Marchattiwar et al. [21] studied the kinetics of DRX during hot compression of 304 austenitic stainless steel and determined the progress of recrystallization fraction from the difference between the generated DRV curve and the experimental DRX curve. Liang Houquan et al. [18] investigated DRX behavior of Ti–5Al–5Mo–5V–1Cr–1Fe alloy and proposed a model to track the DRX process with strain. Sajadifar et al. [22] found that the occurrence of DRX could be determined through the flow stress curves, and the evolution of DRX grain structures could be accompanied by a considerable migration of grain boundaries.

The power dissipation efficiency map, used by many researchers, relates the hot deformation to the power dissipation. It represents how efficiently the power dissipated by microstructure evolution during the hot deformation. With the power dissipation efficiency map, the hot deformation behaviors of different metallic materials have been studied [23–25]. Sang Kyun Oh et al. [26] superimposed the instability map over the power dissipation map to build the processing map. With the processing map, the hot workability of AZ80 Mg alloy was optimized. Fengjun Zhu et al. [27] studied on the hot workability of homogenized 6069 Al alloy cast ingot via hot compression tests. The variation in microstructure was related to the variation in efficiency of power dissipation. They

***Corresponding author: Jingli Zhang,** School of Materials Science and Engineering, Northwestern Polytechnical University, Xi'an 710072, PR China, E-mail: zhangjingli@mail.nwpu.edu.cn
Hongzhen Guo, Houquan Liang, School of Materials Science and Engineering, Northwestern Polytechnical University, Xi'an 710072, PR China

found that DRV was observed in regions associated with the intermediate efficiency of power dissipation, whereas partial DRX occurred in regions with high efficiency. Yu Cao et al. [28] focused on the hot deformation behaviors of H800 alloy. With the efficiency of power dissipation within the range of 35–48 %, H800 alloy exhibited a better workability in deformation temperature range from 975 to 1,100 °C and strain rate from 0.01 to 0.3 s^{-1}.

In this work, the hot compression tests of Ti22Al25Nb alloy under a wide range of deformation temperatures and strain rates have been performed. The effect of microstructural characteristic (such as the second-phase particles) and process parameters (the temperature and strain rate) on the DRX process have been studied. A critical Zener–Hollomon parameter has been proposed to divide conventional dynamic recrystallization (CDRX) from discontinuous dynamic recrystallization (DDRX). The hardening rate of DDRX has been analyzed. And the recrystallization fractions of CDRX and DDRX have been compared. The effect of the second-phase particle on the DRX has been investigated. All these studies are foundations for application of Ti22Al25Nb alloy.

Materials and experimental procedure

Ti22Al25Nb alloy is a kind of Ti–Al–Nb alloys, whose specific chemical composition is given in Table 1. The phase fields of Ti22Al25Nb are: B2 > 1,060 °C, 1,000 °C < α_2 + B2 < 1,060 °C, 975 °C < O + α_2 + B2 < 1,000 °C, 750 °C < O + B2 < 975 °C and O + β < 750 °C [29–31], which were verified by the metallographic method. Figure 1 illustrates the microstructure of the studied Ti22Al25Nb alloy before the hot compression experiment. The darkest phase is the α_2 phase, the lightest phase is B2 and the intermediate contrast phase is O. Note that the O + α_2 particles distribute uniformly within the B2 matrix.

Table 1: Chemical composition of Ti22Al25Nb (wt %).

Ti	Al	Nb	O	N	H
Bal.	22.3	25.7	4.3×10^{-2}	5.2×10^{-3}	9×10^{-4}

Cylindrical specimens with a dimension of ∅8 × 12 mm were machined for tests. A series of isothermal compression tests corresponding to a high reduction of 50 % were conducted by using a Gleebe-1500 thermo simulation machine at five different temperatures (950, 980, 1,010, 1,030 and 1,050 °C) and five different strain rates (0.001, 0.01, 0.1, 1 and 10 s^{-1}). The temperature was controlled within ± 1 °C. Before the experiment, a thermocouple was welded on the center surface of each specimen for accurate temperature control and a tantalum foil was placed between the specimen and anvil for the friction reduction. Each specimen was heated at a heating rate of 10 °C/s to the given deformation temperature and soaked for 3 min to obtain a uniform temperature distribution, then compressed isothermally. After the experiment, the specimen was quenched with water rapidly to preserve the instant microstructure. The specimen was then sectioned along the central axis. The microstructure of the exposed surface polished and etched with the proper solution (HF: HNO_3:H_2O_2:H_2O = 1:2:7:20) was observed by an OLYMPUS-PM3 optical microscope and a Tescan scanning electron microscope.

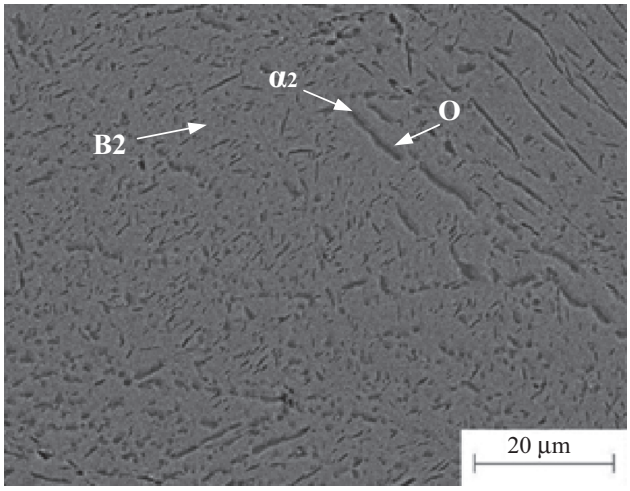

Figure 1: Microstructure of Ti22Al25Nb before the hot compression experiment.

Experimental results and discussion

Flow stress–strain curves of Ti22Al25Nb

Flow stress–strain curves under all the experimental conditions are shown in Figure 2. Note that the curves can be divided into two types: the blue CDRX curves and the red DDRX curves. Figure 3 shows the different deformation mechanisms of CDRX and DDRX.

During the CDRX, the flow stress rapidly increases to the peak in the beginning because of the dislocation

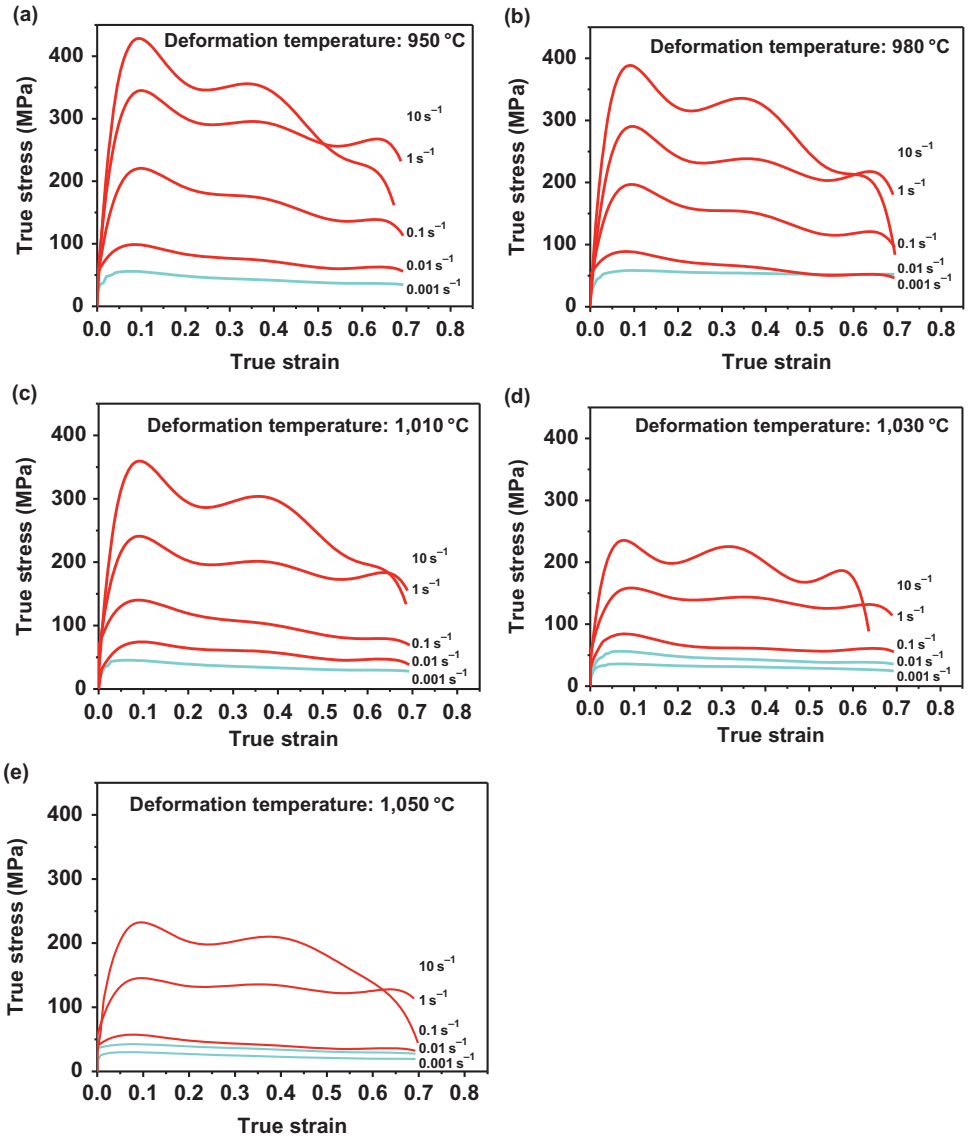

Figure 2: Flow stress–strain curves under all experimental conditions: (a) 950 °C; (b) 980 °C; (c) 1,010 °C; (d) 1,030 °C; (e) 1,050 °C.

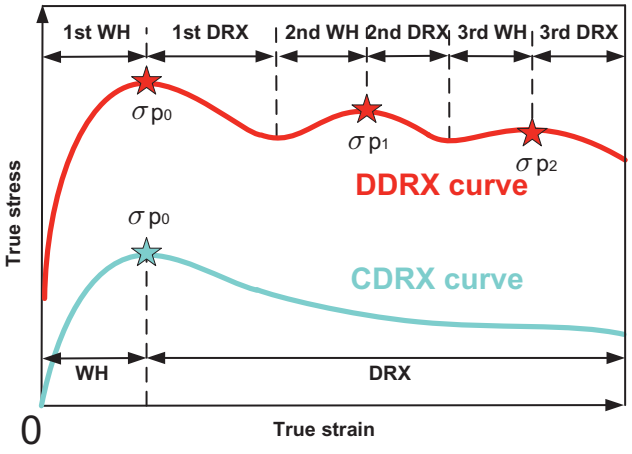

Figure 3: Schematic of the two types of flow curves, which indicates that the CDRX curve is of single peak and DDRX curve is of multi-peak.

intersections and pileups. The DRV is too weak to overcome the WH mechanism, then DRX takes place and the flow stress starts to decrease slowly. When the competition between the hardening and softening mechanism achieves a balance, the flow stress maintains at a fairly constant level regardless of the increasing strain.

During the DDRX, multiple peaks can be found due to the dominance of the hardening mechanism and softening mechanism. The multi-peak curves usually appear at the high strain rates and the low temperatures. Especially at the strain rates of 1–10 s^{-1} and the temperatures of 950–1,030 °C, the multi-peak phenomenon is evident. During the deformation, the α_2 and O phases exhibit different slip characters, compared with some bcc phases. The bcc slip is wavy, but the planar slip is evident in α_2 and O phases [32]. Especially in α_2 phase,

predominant slip systems include $11\bar{2}0$ dislocations on the prismatic $\{10\bar{1}0\}$ plane, which are hardly observed on the basal or pyramidal planes [33]. The limited slip is expected to contribute to the increasing dislocation density leading to the WH. Moreover, the DRX can also be enhanced by the second-phase particles. Following the first DRX, the rapid deformation results in the fast dislocation accumulation. Meanwhile, the high strain rate deformation provides little time for the new recrystallized grains (re-grains) to grow up [34]. The new re-grains are distorted due to the continuous deformation. The rapid dislocation accumulation which results in a raise of the flow stress supplies a driving force for the next DRX. Hence, the alternate dominance of hardening mechanism and softening mechanism appears.

From Figure 2, it can be found that the flow stress–strain curves of Ti22Al25Nb are significantly influenced by the thermal process factors (such as the temperature and strain rate). With the increasing temperature and decreasing strain rate, the multimodal curves become smooth. Hence, the Zener–Hollomon parameter that presents the effects of the temperature and strain rate is considered in the next section.

Constitutive model of Ti22Al25Nb

The constitutive model of the flow stress–strain curves of Ti22Al25Nb during hot deformation process can be characterized by hyperbolic sine law proposed by Sellar and Tegart [35]:

$$\dot{\varepsilon} = A[\sinh(\alpha\sigma)]^n(\exp - Q/RT) \tag{1}$$

where $\dot{\varepsilon}$ is the strain rate (s^{-1}), A, α, n are material constants, Q is the deformation activation energy (kJ mol^{-1}), R is the universal gas constant (8.31 J mol^{-1} K^{-1}). The Zener–Hollomon parameter has been proposed to represent the effects of the temperature and strain rate:

$$Z = \dot{\varepsilon}\exp(Q/RT) = A[\sinh(\alpha\sigma)]^n \tag{2}$$

Taking the logarithm transformation of both sides, eq. (2) can be given as

$$\ln\dot{\varepsilon} + \tfrac{Q}{RT} = \ln A + n\ln[\sinh(\alpha\sigma)] \tag{3}$$

When the temperature keeps constant, taking the partial derivative of $\ln(\sinh(\alpha\sigma))$ in eq. (3), the stress exponent n can be defined as $n = \left\{\frac{\partial\ln\dot{\varepsilon}}{\partial\ln[\sinh(\alpha\sigma)]}\right\}_T$. When the strain rate is a constant, taking the partial derivative of $1/T$, $\frac{Q}{R} = n\left\{\frac{\partial\ln[\sinh(\alpha\sigma)]}{\partial\frac{1}{T}}\right\}_{\dot{\varepsilon}}$. Thus, the deformation activation energy Q can be expressed as

$$Q = R\left\{\frac{\partial\ln\dot{\varepsilon}}{\partial\ln[\sinh(\alpha\sigma)]}\right\}_T\left\{\frac{\partial\ln[\sinh(\alpha\sigma)]}{\partial\frac{1}{T}}\right\}_{\dot{\varepsilon}} \tag{4}$$

Substituting the values of peak stress (σ_p), the curves of $\partial\ln[\sinh(\alpha\sigma)] - \ln\dot{\varepsilon}$ and $\partial\ln[\sinh(\alpha\sigma)] - \frac{1}{T}\times10^3$ can be obtained (see Figure 4).

From Figure 4, we can obtain the value of n and $\frac{\partial\ln[\sinh(\alpha\sigma)]}{\partial\left(\frac{1}{T}\times10^3\right)}$. They are 3.2099 and 20.8619, respectively. Substituting the two values into eq. (4), the value of Q is equal to 556.74 kJ mol^{-1}. Then eq. (2) can be given as

$$Z = \dot{\varepsilon}\exp(556740/RT) = 5.21\times10^{21}\left[\sinh\left(0.00705\sigma_p\right)\right]^{3.21} \tag{5}$$

By taking the logarithm transformation of both sides of eq. (5), the $\ln Z$ can be calculated.

The distribution trend of Zener–Hollomon parameter is shown in Figure 5. The Zener–Hollomon parameter increases with the increasing strain rate and the decreasing temperature. Note that the Zener–Hollomon parameters of CDRX are relatively smaller than those of DDXR. A critical Zener–Hollomon parameter is obtained, which divides CDRX from DDRX. From Figure 5, the critical value $\ln Z_C$ is equal to 47.43. Hence, when $Z \le Z_C$, the curve is CDRX with a single peak; when $Z > Z_C$, the curve is DDRX with multiple peaks. When $Z \le Z_C$, it corresponds to the low strain rate and the high temperature. The storage energy accumulated in the WH process provides driving force for the growth process of new re-grains. Due to the slow strain rate, the re-grains have enough time to grow up. Meanwhile, the migration of grain boundaries can easily occur. In the end of the deformation, the original grains will be replaced by the re-grains completely. Additionally, with the increasing Zener–Hollomon parameter, the size of the re-grains will decrease [36], which can be estimated by $\ln Z$, $\ln d = -k\ln Z + b$ [37], where d is the average re-grain size, k and b are material constants. When $Z > Z_C$, it corresponds to the high strain rate and the low temperature. Due to the fast deformation, the original boundaries will be broken, which provides more nuclei for the re-grains. Meanwhile, the dislocation storage is faster than the dislocation annihilation, which will lead to the high dislocation density in the subgrains. The low different dislocation density between the subgrains and the matrix results in the slow grain boundary mobility. The re-grains are hard to grow up and partial re-grains will be deflated.

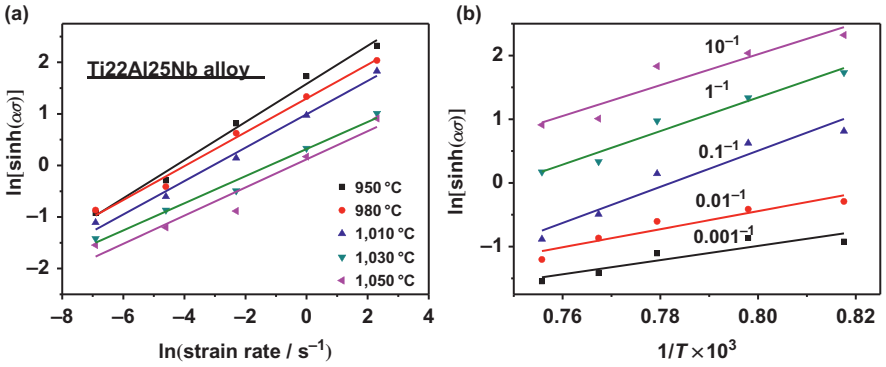

Figure 4: Linear analysis procedure to determine the relationship between peak stress and deformation parameters: (a) $\partial \ln[\sinh(\alpha\sigma)] - \ln\dot{\varepsilon}$ and (b) $\partial \ln[\sinh(\alpha\sigma)] - \frac{1}{T} \times 10^3$.

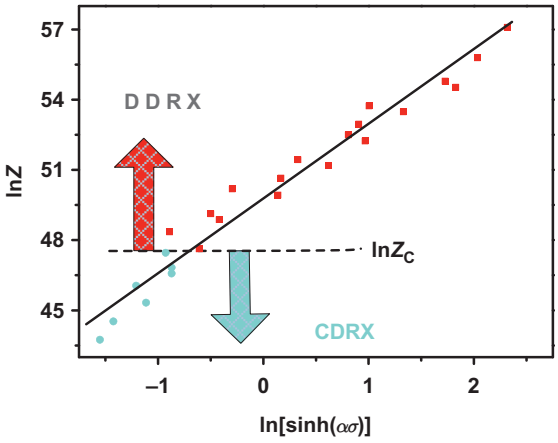

Figure 5: The distribution trend of Zener–Hollomon parameter. The ln Z values can be divided into two parts by the critical value ln Z_C: the DDRX and CDRX.

Discontinuous softening mechanism and DDRX

The hardening rate ($\theta = d\sigma/d\varepsilon$) at the temperature of 1,030 °C is shown in Figure 6(a). In the beginning of the deformation process, the WH mechanisms, such as dislocation intersections and pileups [18, 38], lead to the positive θ value. The softening mechanism is hard to overcome the WH. With the continuous deformation, the DRX takes place, resulting in the decreasing θ value. When the DRX becomes the dominant deformation mechanism, the θ value falls to negative. It can be found that the DRX mechanism of Ti22Al25Nb is significantly influenced by the strain rate at a given temperature. At the low strain rate (0.001 and 0.01 s^{-1}), the specimen exhibited the normal hardening rate curve. At the high strain rate (0.1, 1 and 10 s^{-1}), the hardening rate curve of DDRX can be divided into multiple stages (see Figure 6(b)). When the DRX dominated the deformation mechanism instead of WH, the θ changed from positive to negative. Afterward, the continuous deformation at high strain rate led to the rapid dislocation accumulation and the distortion of the new re-grains. When the softening mechanism was too weak to overcome the hardening mechanism, the θ increased to the positive value. The above process repeated several times, which is different from that of CDRX.

Figures 7 and 8 illustrate the typical microstructures of Ti22Al25Nb alloys compressed at the high strain rate and low strain rate, respectively, at 1,030 °C. In Figure 7, the black lines highlight the original grains. It is noted that the original grain boundaries did not disappear and numbers of small re-grains nucleated along the original grain boundaries. Furthermore, the faster the strain rate was, the more re-grains could be observed. The rapid hot deformation led to the fast dislocation accumulation which was hardly weakened by the slow dislocation annihilation. The fast dislocation accumulation provided enough driving force for the DRX nucleation. When the dislocation density reached a critical level, the DRX took place and some new re-grains appeared, which resulted in the temporary decreasing of stress. Then the original big grains and some re-grains were elongated by the rapid continuous deformation which accelerated a new WH. Figure 8 shows the microstructures of the specimens deformed at the strain rate of 0.01 and 0.001 s^{-1}. The Ti22Al25Nb alloys underwent the conventional hardening and softening process (see the inset of Figure 6(a)). During the slow deformation, the new re-grains grew up gradually. Eventually, the original grains were entirely replaced with the grown re-grains, then a equiaxed microstructure was formed.

The differences of volume fraction curves between CDRX and DDRX are shown in Figure 9. The volume

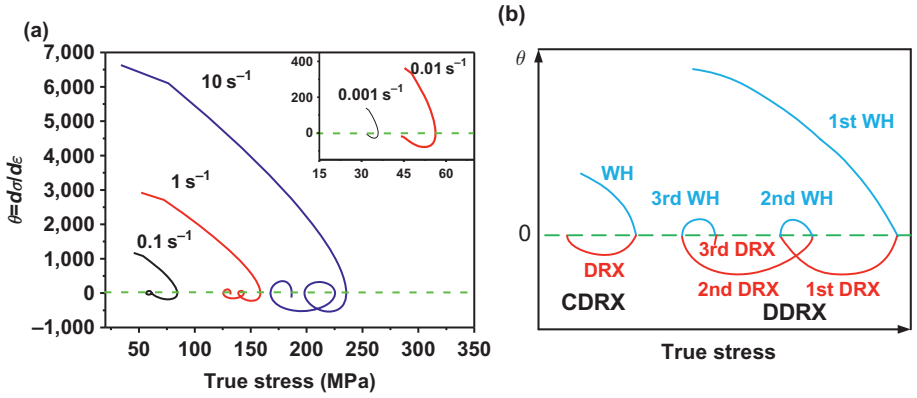

Figure 6: (a) Hardening rate of the specimens at the temperature of 1,030 °C and (b) schematic of the hardening rate curves of the two types of DRX.

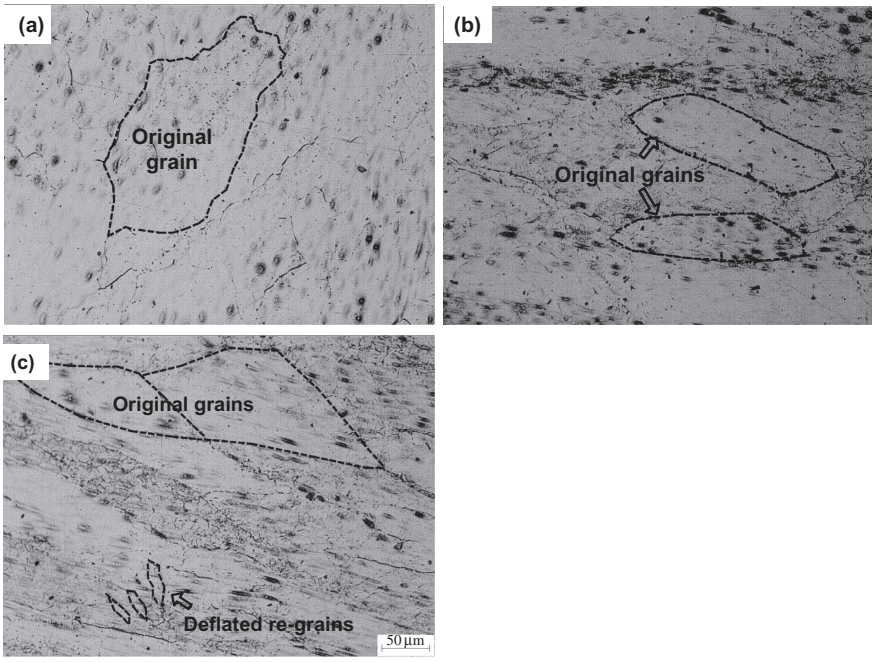

Figure 7: Microstructure evolution under the temperature of 1,030 °C and the strain rates of (a) 0.1 s^{-1}, (b) 1 s^{-1} and (c) 10 s^{-1}.

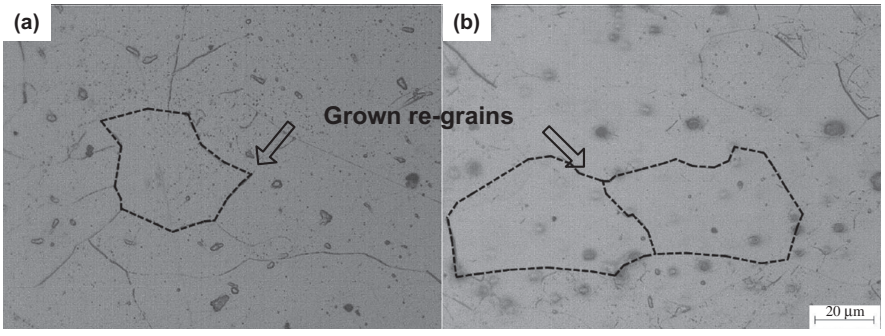

Figure 8: Microstructure evolution under the temperature of 1,030 °C and the strain rates of (a) 0.01 s^{-1} and (b) 0.001 s^{-1}.

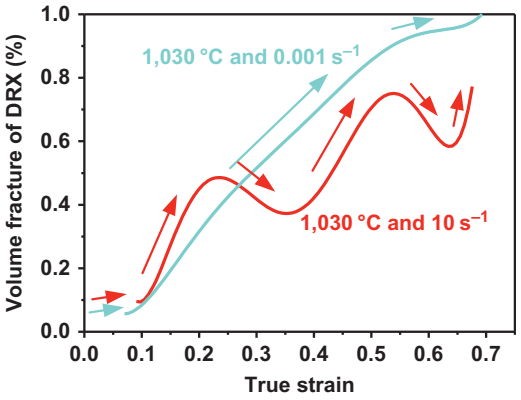

Figure 9: Volume fraction of DRX under the conditions of (a) 1,030 °C and 0.001 s^{-1} and (b) 1,030 °C and 10 s^{-1}. (The blue curve and red curve illustrate the CDRX and DDRX types, respectively.)

fraction curve of CDRX under the condition of 1,030 °C and 0.001 s^{-1} is a normal S-curve, which increases with the increasing strain rate (blue curve in Figure 9). During the low strain rate deformation, the specimen underwent a stable DRX process. The slow deformation process provided enough time for the re-grains to nucleate and grow. Finally, the volume fraction of DRX reached 100 %, which indicated the complete occurrence of CDRX. The volume fraction curve of DDRX under the condition of 1,030 °C and 10 s^{-1} (red curve in Figure 9) is a wave-shaped one, which displays rise–decline–rise property. The ascendant line indicates the DRX process, while the descendant line represents the second and third WH processes. In the declining part of the curve, the hardening rate θ changed from negative to positive and the flow stress increased. In the end, the original grains were not replaced in the material. Hence, the final volume fraction of DDRX is lower than that of CDRX.

Effect of second-phase particles on the DRX

During the hot deformation process, the effect of second-phase particles on the DRX is obvious. Figure 10 illustrates the microstructure evolution at the low strain rate of 0.001 s^{-1}. At the temperature of 950 °C (in the $O + \alpha_2 + B2$ phase field), O and α_2 particles distributed uniformly within the B2 matrix (see Figure 10(a)). When deformed at the low strain rate, the re-grains were inclined to nucleate at the original boundary or near the second-phase particles. Additionally, the grain boundary migration was restrained by the second-phase particles (indicated by the black arrows). In the end, a microstructure of fine re-grains was obtained. At the temperature of 1,010 °C (in the $\alpha_2 + B2$ phase field), partial O particles dissolved, and the volume fraction of second-phase particles decreased (see Figure 10(b)). Note that when the distance between particles was short, the new re-grains were restrained growing. In the area where the particles

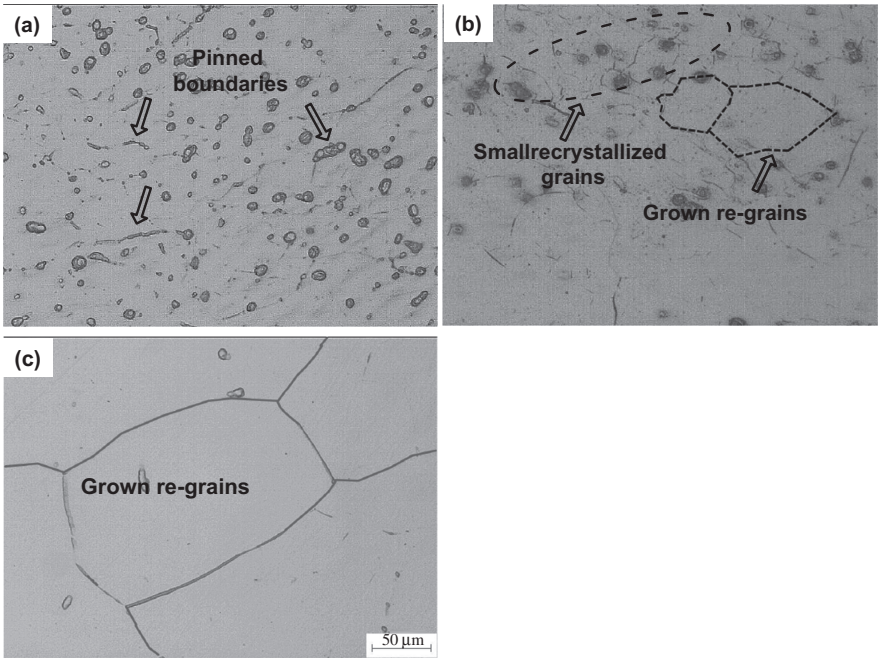

Figure 10: Microstructures of the specimens at the strain rate of 0.001 s^{-1} and the temperatures of (a) 950 °C, (b) 1,010 °C and (c) 1,050 °C, which reveal the effect of second-phase particles on the growing process of re-grains.

distribute sparsely, some grown re-grains are observed. When the temperature rose to 1,050 °C (close to the B2-transus), the pinning force of the second-phase particles was too weak to hold the grain boundaries (see Figure 10 (c)). Then the grains grew up gradually, whose average size increased to 78 μm. Figure 11 shows the relationships between the microstructural parameters and the temperature at the strain rate of 0.001 s^{-1}. With the increasing temperature, the pinning force of the second-phase particles on the grain boundary decreased, which resulted in final coarse equiaxed grains.

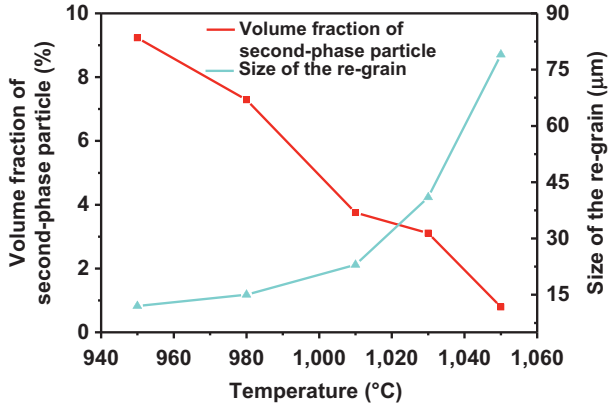

Figure 11: Relationships between the microstructural parameters and the temperature at the strain rate of 0.001 s^{-1}.

Figure 12 illustrates the microstructure evolution at the high strain rate of 1 s^{-1}. At the temperature of 950 °C, there are many α_2/O phases precipitated in the B2 matrix (see Figure 12(a)). On the one hand, dislocations piled up around the second-phase particles at the high strain rate, which would lead to the WH process. On the other hand, due to the differences of plasticity and elasticity between the matrix and second-phase particles, the local lattice distortion occurred close to the phase interfaces. Hence, the DRX would easily take place in this high dislocation density area. Lots of recrystallized nuclei were found around the second-phase particles, while *few* of re-grains can be observed, which indicates the high nucleation rate and the low growth rate of DDRX. At the temperature of 1,010 °C, some second-phase particles dissolved. Partial re-grains are found nearby the second-phase particles. Meanwhile, the serrated original boundaries indicated the nucleation of the other part of re-grains (see Figure 12(b)). When the temperature reached 1,050 °C, the volume fraction of second-phase particle was less than 1% (see Figure 11). Thus, the effect of second-phase particle on the DRX can be disregarded. In Figure 12(c), the re-grains mainly nucleated along the boundaries. The driving force for the DRX was only supported by the dislocation accumulation within the matrix and the re-grains.

Through above comparison and analysis, under the condition of the high strain rate, the second-phase particles have an important impact on the DDRX process. When more second-phase particles precipitated in the matrix, the DDRX process would be enhanced. It is agreed with the change trend of the flow stress–strain curves in Figure 2 that the multi-peak phenomenon is more notable at the low temperature.

Power dissipation efficiency map

The dynamic material modeling (DMM), which was developed by Prasad et al. [39], is an effective method to correlate the workability with the thermomechanical parameters based on the irreversible thermodynamics, continuum mechanics and physical systems simulation. Based on DMM, the specimen undergoing high-temperature deformation can be considered as power dissipation with the assumption that the workpiece and the whole deformation system act as a closed adiabatic system. The total power dissipation (P) during hot deformation can be divided into two parts: the power dissipated by plastic deformation (G) and the power dissipated by microstructure evolution (J), which can be defined as

$$P = \sigma\dot{\varepsilon} = G + J = \int_0^{\dot{\varepsilon}} \sigma d\dot{\varepsilon} + \int_0^{\sigma} \dot{\varepsilon} d\sigma \tag{6}$$

The power dissipation efficiency η represents how efficiently the power was dissipated by microstructure evolution, which is a function of the strain rate sensitivity m:

$$\eta = \frac{J}{J_{\max}} = \frac{2m}{m+1} \tag{7}$$

where m is the strain rate sensitivity, $m = dJ/dG = \partial(\ln\sigma)/\partial(\ln\dot{\varepsilon})$. The power dissipation map can be established by the values of η at different temperatures and strain rates at a given strain.

The power dissipation efficiency map for hot deformation process of Ti22Al25Nb alloy at the strain of 0.7 is displayed in Figure 13. In general, the power efficiency is higher in the CDRX domain. The higher power dissipation efficiency indicates that more power are consumed by microstructure evolution. DRX behavior has been considered as an energy-cost process, owing to the new grain nucleation and boundary migration. Due to

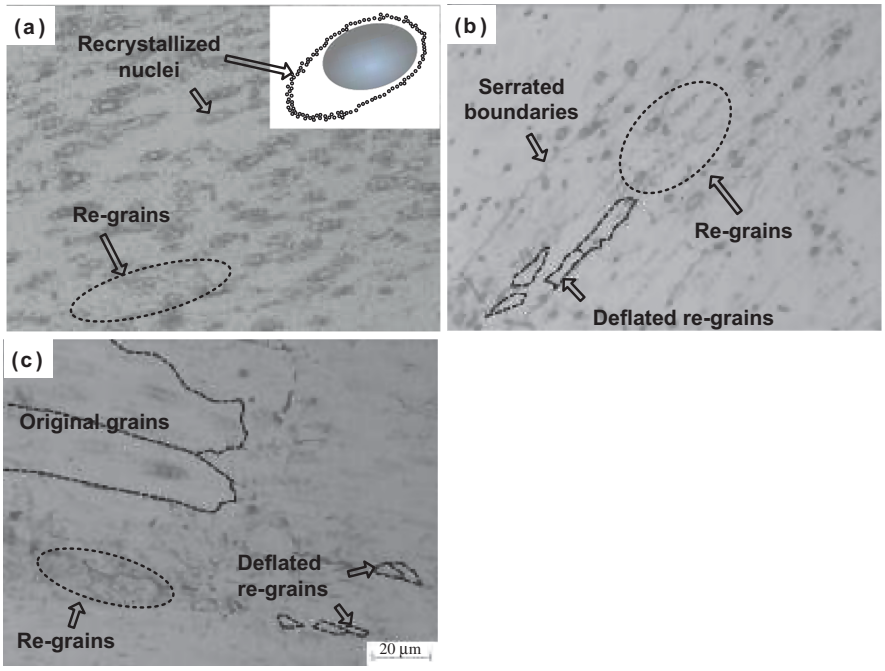

Figure 12: Microstructures of the specimens at the strain rate of 1 s^{-1} and the temperatures of (a) 950 °C, (b) 1,010 °C and (c) 1,050 °C, revealing the different recrystallization nucleation mechanisms during the fast hot deformation.

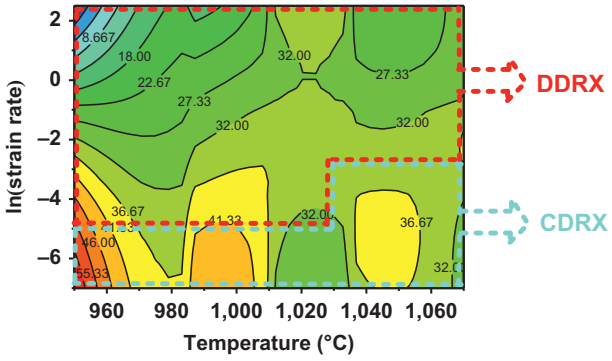

Figure 13: Power dissipation efficiency map for hot deformation process of Ti22Al25Nb alloy at the strain of 0.7. The CDRX domain and DDRX domain are indicated by the blue line and red line, respectively.

the complete DRX behavior, the power dissipation efficiency of the material exhibits a high value during the CDRX process, which is agreed with the previous works [38]. During the DDRX process, more power will be dissipated by the plastic deformation. As a result, the power dissipation efficiency is lower than that of CDRX. The lower power dissipation efficiency indicates the incomplete DRX process and the low DRX volume fraction. The power dissipation efficiency map gives an excellent match with the microstructure evolution which has been shown above.

Conclusion

The DRX of Ti22Al25Nb alloy has been studied under wide ranges of forming *temperatures* and *strain rates* and these conclusions could be drawn as follows:

1. The true stress–strain curves of Ti22Al25Nb can be divided into two types: the CDRX curve and DDRX curve. A critical Zener–Hollomon parameter Z_C has been proposed. When $Z \leq Z_C$, the curve is CDRX which has a single peak. The DRX may occur completely and the original grains will be replaced by the new re-grains; when $Z > Z_C$, the curve is DDRX which has multiple peaks. The re-grains are hard to grow up, especially at the low temperature and high strain rate.
2. Multiple alternate dominance of hardening and softening mechanisms can be reflected by the hardening rate curves of DDRX. When the DRX dominates the deformation mechanism, the value of θ changes from positive to negative. With the rapid continuous deformation, the softening mechanism is too weak to overcome the hardening mechanism and θ increases to the positive value.
3. The volume fraction of CDRX is a normal S-curve and the volume fraction of DDRX is a wave-shaped curve, which displays rise–decline–rise property. The final recrystallization fraction of the CDRX microstructure

is higher than that of the fully equiaxed DDRX microstructure.

4. The effect of second-phase particles on the DRX is obvious. With the increasing temperature, the volume fraction of second-phase particles reduces and the size of final equiaxed grains increases.
5. The power dissipation efficiency map for hot deformation process of Ti22Al25Nb alloy at the strain of 0.7 has been established, which matches with the microstructure evolution.

References

[1] D. Banerjee, Prog. Mater. Sci., 42 (1997) 135–158.
[2] B. Mozer, L.A. Bendersky and W.J. Boettinger, Scr. Metall. Mater., 24 (1990) 2363–2368.
[3] L. Germann, D. Banerjee, J.Y. Guédou and J.L. Strudel, Intermetallics, 13 (2005) 920–924.
[4] Q.M. Wang, K. Zhang, J. Gong, Y.Y. Cui, C. Sun and L.S. Wen, Acta Mater., 55 (2007) 1427–1439.
[5] S.Q. Li, Y. Mao, J.W. Znang, J.T. Li, Y.J. Cheng and Z.Y. Zhong, Trans. Nonferrous Met. Soc. China, 12 (2002) 582–586.
[6] H. Wu, P. Zhang, L. Wang, H. Zhao and Z. Xu, Appl. Surf. Sci., 256 (2009) 1333–1340.
[7] C.J. Boehlert, Metall. Mater. Trans. A., 32 (2001) 1977–1988.
[8] C. Qin, Z.-K. Yao, Y.-Z. Li, Y.-Q. Ning and H.-Z. Guo, Trans. Nonferrous Met. Soc. China, 24 (2014) 3500–3508.
[9] L. Tan, Z. Yao, C. Qin, H. Guo and J. Zhang, Chin. J. Nonferrous Met., 20 (2010) 1533–1538.
[10] L. Tan, Z. Yao, W. Zhou, H. Guo and Y. Zhao, J. Plasticity Eng., 17 (2010) 130–134.
[11] C.J. Boehlert, B.S. Majumdar, V. Seetharaman and D.B. Miracle, Metall. Mater. Trans. A, 30 (1999) 2305–2323.
[12] Y.-J. Cheng, S.-Q. Li, X.-B. Liang and J.-W. Zhang, Trans. Nonferrous Met. Soc. China, 16 (2006) S2058–S2061.
[13] M. Hagiwara, A. Araoka, S.J. Yang, S. Emura and S.W. Nam, Metall. Mater. Trans. A, 35A (2004) 2161–2170.
[14] F. Tang and M. Hagiwara, J. Mater. Res., 17 (2002) 2611–2614.
[15] M. Apel, B. Boettger, J. Rudnizki, P. Schaffnit and I. Steinbach, ISIJ Int., 49 (2009) 1024–1029.
[16] K. Chang, W. Feng and L.-Q. Chen, Acta Mater., 57 (2009) 5229–5236.
[17] Y. Gao, H. Zhang, X. Jin, C. Huang and Z. Luo, Acta Metall. Sin., 45 (2009) 1190–1198.
[18] H. Liang, H. Guo, Y. Ning, X. Peng, C. Qin, Z. Shi and Y. Nan, Mater. Des., 63 (2014) 798–804.
[19] H. Mirzadeh and A. Najafizadeh, Mater. Des., 31 (2010) 1174–1179.
[20] H. Mirzadeh and A. Najafizadeh, Mater. Des., 31 (2010) 4577–4583.
[21] A. Marchattiwar, A. Sarkar, J.K. Chakravartty and B.P. Kashyap, J. Mater. Eng. Perform., 22 (2013) 2168–2175.
[22] S.V. Sajadifar, M. Ketabchi and B. Bemanizadeh, Metallurgist, 56 (2012) 310–320.
[23] X. Peng, H. Guo, Z. Shi, C. Qin, Z. Zhao and Z. Yao, Mater. Sci. Eng. A, 605 (2014) 80–88.
[24] Y.C. Lin, L.-T. Li, Y.-C. Xia and Y.-Q. Jiang, J. Alloys Compd., 550 (2013) 438–445.
[25] Y.Q. Ning, Z.K. Yao, Z. Yang, H.Z. Guo and M.W. Fu, Mater. Sci. Eng. A Struct. Mater., 531 (2012) 91–97.
[26] S.K. Oh, K.K. Lee, Y.-S. Na, C.H. Suh, Y.-C. Jung and Y.S. Kim, Int. J. Precis. Eng. Manuf., 16 (2015) 1149–1156.
[27] F.-J. Zhu, H.-Y. Wu, M.-C. Lin, S. Lee and W.-R. Wang, J. Mater. Eng. Perform., 24 (2015) 2051–2059.
[28] H.D. Yu Cao and J. Zhang, Acta Metall. Sin., 49 (2013) 811–821.
[29] W. Wang, W. Zeng, C. Xue, X. Liang and J. Zhang, Mater. Sci. Eng. A, 603 (2014) 176–184.
[30] H.Y. Zhang Yonggang, C. Guoliang, G. Jianting, W. Xiaojing and F. Di, Structural Intermetallics, National Defense Industry Press, Beijing (2001).
[31] T. Hongjie, Research on Preparation Process of Ti2AlNb/Ti60 Dual Alloy, Northwestern Polytechnical University, Xi'an (2013), pp. 47.
[32] C.J. Boehlert, B.S. Majumdar, S. Krishnamurthy and D.B. Miracle, Metall. Mater. Trans. A, 28 (1997) 309–323.
[33] D. Banerjee, Philos. Mag. A, 72 (1995) 1559–1587.
[34] Y.C. Lin, X.-M. Chen, D.-X. Wen and M.-S. Chen, Comput. Mater. Sci., 83 (2014) 282–289.
[35] C.M. Sellars and W.J. McTegart, Acta Metall., 14 (1966) 1136–1138.
[36] A. Bartels, H. Kestler and H. Clemens, Mater. Sci. Eng. A, 329–331 (2002) 153–162.
[37] L. Yong and T. Huiping, Powder Metallurgical Titanium Base Structural Materials, Central South University Press, Changsha (2012).
[38] H. Liang, H. Guo, Y. Nan, C. Qin, X. Peng and J. Zhang, Mater. Sci. Eng. A, 615 (2014) 42–50.
[39] Y. Prasad, H.L. Gegel, S.M. Doraivelu, J.C. Malas, J.T. Morgan, K. A. Lark and D.R. Barker, Metall. Trans. A Phys. Metall. Mater. Sci., 15 (1984) 1883–1892.